On the fracture of multi-crystalline silicon wafer

Lv Zhao, Daniel Nelias,* Didier Bardel, Anne Maynadier,† and Philippe Chaudet
Univ Lyon, INSA-Lyon, CNRS UMR5259, LaMCoS, F-69621, France.

Benoit Marie
Univ. Grenoble Alpes, INES, F-73375 Le Bourget du Lac, France. CEA, LITEN, Department of Solar Technologies, F-73375 Le Bourget du Lac, France.

(Dated: September 5, 2016)

This work focuses on the fracture behavior of multi-crystalline silicon in 4-point bending test. The objective is to investigate the crack path as well as the effect of the grain boundary on the crack propagation. Thin specimens that contain the same grains have been tested under identical loading in order to assess the consistency of the fracture process. A fractography analysis has been carried out with a confocal microscope to describe the crack propagation within grains and at grain boundaries. The fracture paths have been also compared to X-FEM numerical simulations, and a very good agreement was found. Fractographies have been used to identify the cleavage planes in locations where surface instabilities are observed, and to reveal how grain boundary are crossed. Laue X-ray diffraction analysis has been carried out to measure the grain orientations and further identify the cleavage planes in the areas far from instabilities and grain boundaries. It is observed that the fracture of multi-crystalline silicon is completely determinist, i.e. same crack path for twin silicon plates, with the crack propagating mainly on the crystallographic plane (111) and eventually on (110). The misorientation across the grain boundary can drive the crack away from the lowest surface energy plane. Another interesting observation is that the grain boundary slows down or stops shortly the crack propagation.

I. INTRODUCTION

Crystalline silicon wafers are used in many industrial applications such as microelectromechanic systems (MEMS) and photovoltaic cells. As the silicon is a very brittle material at temperature below 600°C [1, 2] – which is above most of the service temperatures, brittle fracture is always a major concern from both manufactures and users point of view.

The fracture of single crystalline silicon (SCSi) has been widely investigated both experimentally and numerically. The anisotropic behavior in terms of fracture plane and direction has been reviewed by Cox et al. [3]. It has been shown that the fracture arises predominantly on cleavage plane either (111) or (110) in experimental investigations [4, 5] and numerical works [6–8], because of the low surface energy of these specific planes. Correspondingly, the fracture toughness has been largely assessed using different experimental methods, such as macroscopic tensile tests [9], microscopic tensile tests [5] as well as Vickers microhardness indentation [10]. The results indicated that the (111) plane is more favorable energetically for cleavage. Particularly, the anisotropy in cracking direction has been experimentally highlighted, especially, the fracture along the $\langle 100 \rangle$ direction in the (110) plane can not be achieved. Experimental observations have revealed a systematical deflection towards the (111) plane in this case [10, 11]. This finding makes the general Griffith criterion invalid, since the latter only relies on the surface energy without distinction over the in-plane directions. Elucidation for this deflection phenomenon has been provided thanks to quantum mechanical calculations [12], which highlight that the bond breaking process is discontinuous and can cause a large lattice trapping [13] for crack propagation along the $\langle 100 \rangle$ direction in the (110) plane. Interestingly, Sherman and Be'ery [11] have shown that a propagating crack in the (110) plane along the $\langle -110 \rangle$ direction may also jump to the (111) one when the crack propagation velocity is high. This abnormal behavior seems to have no relation with lattice trapping and was interpreted as linked to a dynamic crack propagation phenomenon. Moreover, the works from this group [14] have reported special surface instabilities on the (111) fracture surface in bending loading. This phenomenon has been recently demonstrated to be initiated at dopants [15].

Regarding the aggregate of multiple silicon single crystals separated by grain boundaries, a distinction should be made between poly-crystalline silicon (PolySi) and multi-crystalline silicon (MCSi). Both have been much less studied for fracture behavior than mono-crystalline silicon. PolySi are essentially used in MEMS, with grain size in the order of micro- or nano-meters, whereas MCSi are employed in the photovoltaic (PV) domain. For the latter the solidification process is well controlled in order to get millimetric to centimetric length size grains, which is almost of the same order of magnitude than the dimension of the structure. The objective is to reduce the grain boundaries which are harmful to the electrical efficiency. Considered as crystal surface defects, the grain boundaries are very complicated structures that are usually described by a tilt and a twist angles [16]. The atomic ar-

* daniel.nelias@insa-lyon.fr
† Now at Femto-ST, F-25030 Besanon, France

rangements in these regions are highly disturbed by the presence of geometrically necessary dislocations (GNDs) [17] and stacking faults. With these crystal defects, it seems that the crack would take place more easily along the grain boundaries than on the trans-granular cleavage planes. However, it has been highlighted, both by experiments and modeling, that an important interaction takes place between a crack and dislocations which induces local instability (deflection) on the fracture path [14, 18]. Thus, the propagating crack would be quite unstable if it goes through a grain boundary. Indeed, some authors have supposed that the fracture of multi-crystalline silicon can be inter-granular. Paggi et al. [19] and Infuso et al. [20] have performed some numerical studies with cohesive zone model (CZM) to investigate fracture of silicon. Coffman and James [21] have carried out molecular dynamic simulations to assess the surface energy of the grain boundaries in function of the misorientation. However, the real fracture toughness by experimental measurements is not available in the literature. It should be noted that inter-granular fracture of PolySi or MCSi has not been experimentally observed, to the best of the authors' knowledge. In the other hand, transgranular fracture for PolySi [22] has been reported both by experiments and CZM simulations. In our former work [23], based on the fracture of more than 100 silicon wafers, only transgranular cracks have been observed.

Assuming a transgranular crack in PolySi and MCSi, will it propagate on the same cleavage planes as for silicon single crystal? This question has never been properly answered. Brodie and Bahr [24] have shown wild fracture surface roughness for PolySi at room temperature, while the cleavage plane characteristic has not been addressed. Mulay et al. [22] have indicated that PolySi fracture surface follows approximately the (111) plane according to the grain orientation texture, yet further verification has not been conducted. It has also been experimentally observed that cracks are likely to initiate on the (111) plane for solar grade MCSi [23]. However, upon crossing the grain boundary, will the crack be perturbed by the latter? Indeed, Gerberich et al. [25] has revealed the grain-boundary-affected-zone in which the crack-tip stress field is distorted. Fractographies have shown that the crack crosses the grain boundary with discontinuous steps in uni-axial tensile configuration [26–28], which suggests that the grain boundary tends to increase locally the fracture toughness and pin the crack front. The barrier effect induced by an important twist misorientation at the grain boundary has also been highlighted in a recent work [29]. In such a situation the applied stress should increase in order to unpin the crack front.

As a summary of the literature review, (i) the grain orientation drives the fracture path within each grain due to the anisotropy of the crystal, (ii) the grain boundary strongly affects the crack propagation when it jumps from one grain to the next one, and (iii) the brittle behavior of crystalline silicon results in a dynamic fracture process. However dynamics effects are still not clearly understood. For example the fact that cracks propagating at a very high speed may switch from the (110) plane to the (111) plane has not been confirmed. Then how does fracture of silicon multi-crystal proceed in grains and across the grain boundaries? Would the effect of the grain boundary relate strictly to the misorientation? Is the fracture process experimentally reproducible?

In order to address the above questions, a set of photovoltaic grade multi-crystalline silicon plates have been tested until fracture with a 4-point bending apparatus. The specimens have been extracted from silicon ingot cast with wire sawing (to produce wafers of thickness around 170 μm) and then laser cut to obtain square specimens of size 50×50 mm. The advantage of using this kind of technique is that we can get twin specimens, i.e. two different plates with very similar grain morphology since cut nearby in the same ingot. So it is interesting to compare the fracture behaviors of two almost identical specimens under the same loading. For each of them a pre-crack has been created at the same location, before to undergo 4-point bending until fracture. A high speed camera was set up to track the crack propagation. After cracking, the overall fractography was carried out to study the crack surface morphology. In order to correlate the crack paths with the crystallographic orientations of the grains, measurements by the Laue X-ray diffraction were carried out.

Lastly a numerical model has been built based on the extended finite element method (X-FEM). The initial plane where the crack starts to propagate is chosen among one of the lowest energy planes for cleavage. A cohesive zone energy release criterion is then choosen to control the fracture propagation. Numerical results will then be compared to experimental data.

II. MATERIALS AND EXPERIMENTAL METHODS

A. Multi-crystalline silicon plates

The specimens are laser cut from solar grade multicystalline silicon wafers into square plates with surface dimension of 50 × 50 mm. The thickness of the latter corresponds to that of the wafer and measures around 170 μm. A remarkable characteristic for the solar grade silicon is that the grains are generally millimeter to centimeter large, with the grain boundaries visible with the naked eye. Inside the grains, one can observe frequently a couple of twin boundaries in the form of long strips. As a symmetric plane of a crystal lattice, the twin boundary is demonstrated to belong to the {111} family in this study, as illustrated below in Fig. 1 presenting preliminary EBSD measurements on one randomly chosen specimen. The conclusion is consistent with that reported in the literature [30].

From the color code maps associated with the inverse pole figure, one can find clearly that the twin changes

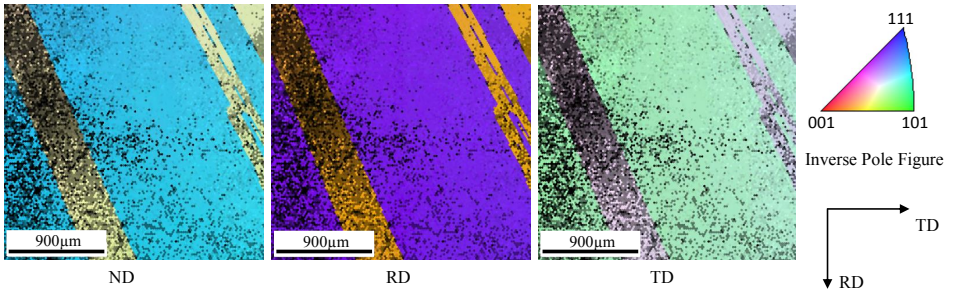

(a)

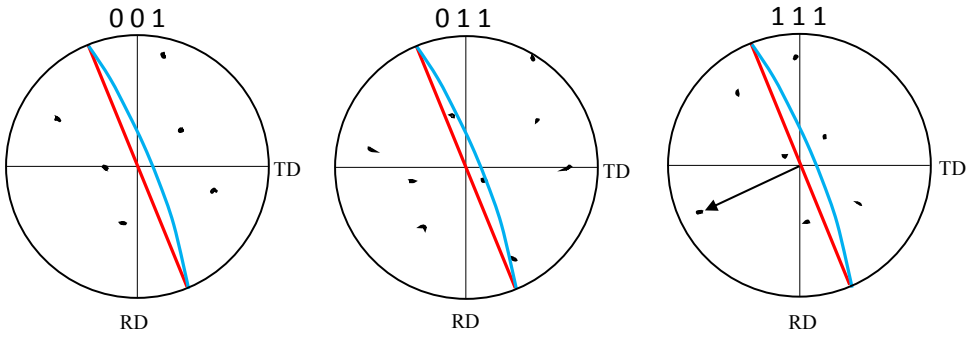

(b)

FIG. 1: Twin boundary characteristic: color coded map (a) and corresponding pole figures (b). The red straight line denotes the twin boundary supposed perpendicular to the specimen's surface as presented in the color code map, the blue curved line represents the the projection of the real twin boundary obtained with the symmetry of the poles.

locally the crystallographic orientation. In all the three corresponding pole figures, a symmetric crystalline structure can be easily revealed (a twin boundary is a symmetric plane within a crystal lattice). The red straight line denotes the approximate twin boundary that is supposed perpendicular to the specimen's surface, while the blue curved line represents the symmetric plane and therefore the real twin boundary. From Fig. 1b, it can be noticed in the [110] pole figure that the twin boundary contains three [110] directions. As complementary, in the [111] pole figure, one can observe that one [111] direction is almost perpendicular to the twin boundary. With the above analysis, it can be confirmed that the twin boundary belongs to the {111} family.

Due to the small thickness of the silicon wafers compared to the grain size, we can obtain almost twin or triplet wafers when wafers are laser cut in a row in a silicon ingot. An example of two plates containing the same grain shapes and orientations is presented in Fig. 4. It is then possible to investigate the fracture behavior of twin specimens under the same or for different loading conditions.

In order to avoid multi-cracks or crack bifurcation as encountered in a former study [23], a pre-crack or local defect has been introduced with a Vickers indenter at the center of one of the specimen edges as presented in Fig. 2. The induced notch is about 130 µm long. The dark stain on the left side of the notch is the positioning mark. Particularly, the twin wafers possess the same pre-crack spot. Note that the pre-crack dimension results in a fracture stress of approximately 35 MPa.

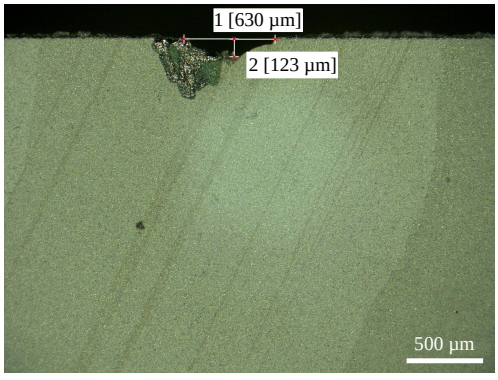

FIG. 2: Precrack carried out with a Vickers pointer. The position of the pre-crack is spotted by a dark stain (on the left of the notch) for consistency between twin plates.

B. Bending tests with high speed imaging technique

The studied silicon plates are thin (thickness around 170 µm) and brittle. Classical uniaxial tensile tests are difficult to perform due to gripping and alignment issues. However, the 4-point bending test is a good alternative because of its simplicity and also because it produces a uniform tensile area at the lower surface in the area between the two inner support cylinders. Besides, the fracture surface contains more useful information under bending compared to that under uniaxial tension, such as the surface instabilities as mentioned in the introduction [31]. The parameters of our experimental set up are given in Table I. The outer and inner spans correlate well with the recommendations in ASTM C 1161-02c [32]. The punch and support rollers are in steel, and of low roughness to avoid local stress concentration at the contact interface. The tests were performed at constant punch velocity with a LLOYD-Ametek LFPLUS electro-mechanical machine. The cross-head moving down rate was 0.2 mm/min, which implies a strain rate in the order of $10^{-6}\mathrm{s}^{-1}$ and thus a quasi-static loading. An integrated displacement sensor provides in real time the punch displacement, and an external force sensor with a capacity of 10 N is used to measure the reaction force on the punch.

TABLE I: Parameters of experimental set up (schematized in Fig. 3)

Inner span	Outer span	Punch roller radius
a=21 mm	d=40 mm	r=3 mm

The high speed imaging technique has been used to track the fracture process knowing that the crack propagation velocity is very high. The used high speed camera (Phantom V710) was set with a frequency of 49,000 Hz and a resolution of 256×512 pixels for all the tests. A manual trigger allowed to save the last 2 seconds of the high speed camera so that the fracture can be entirely captured. Since the specimen should be horizontally placed on the support rollers, a tilted mirror was set up under the specimen which allowed the camera to image the tensile surface of the specimen. Figure 3 provides a comprehensive illustration for the depicted configuration. It should be noticed that the observation region is reduced (50 mm to 25.6 mm) but the pure bending area is still fully covered, since the inner contact span is 21 mm.

Several pairs of twin plates have been investigated. The test results and the analysis will be addressed in detail mainly for one pair of twin plates (see Fig. 4) for which the reproducibility is revealed. Another 2 pairs turned out similar results, while the rest pairs resulted in deviated fracture paths due to either inconsistent pre-cracks or slightly different grain distributions.

III. FRACTURE PATH INVESTIGATION

A. Surface imaging analysis

The cracking results of two twin plates are displayed in Fig. 4. The first remarkable observation is that the fracture paths are highly similar from the begin to the end of the cracking (here from top to bottom). Other outputs of interest are:

i) Unlike isotropic brittle materials, the crack does not align with the maximal principal stress plane, which corresponds to the bending axis, here the vertical direction in Fig. 4.

ii) Intergranular propagation is not observed. The crack goes straightly in the grains and then changes its direction upon crossing grain boundaries.

iii) In the two mentioned images, one can notice that the crack aligns with the twin boundaries in the biggest grain at the plate center, which represents a (111) plane, as discussed in our EBSD analysis (see Fig. 1).

From these observations, it can be concluded that the fracture of the multi-crystalline silicon is reproducible and the crack propagates in trans-granular way probably on low energy planes like (111) or (110).

Regarding the high speed imaging, the subtraction between two consecutive images highlights the crack propagation. To properly detect the crack tip, the contrast is reinforced with a wavelet denoising. Even if this method presents some uncertainties, it gives a relevant estimation of the crack growth during the cracking process. The main drawback is linked to the acquisition frequency which is limited, leading to a laps time of about 20µs between two images. That affects straightly the estimation of the crack propagation velocity which is an average during the laps between two consecutive images. However, in this study, this technique allows to correlate the crack velocity and the crack path, especially the step changes of the propagation velocity when the crack crosses the grain boundary. As presented in Fig. 5, the reference image is one on the completely cracked specimen which helps to figure out the entire propagation path on the sample surface. The next image, first of a series of 7, corresponds to the subtraction between the first photo after cracking and the prior one just before cracking, revealing the starting crack. The following images are also done by subtracting the image at the current time step by the one just before cracking, until the crack covers the specimen.. The yellow marks spot the crack tip positions at each time step. After each subtraction, an instantaneous crack length can be measured at each time step. According to the sample frequency (49, 000 Hz), i.e. 20 µs between two successive images, the mean crack propagation velocity can be calculated as plotted Fig. 6.

The propagation in multicrystalline silicon is relatively slow (400 m/s in average) compared with the reported steady state velocity which is about 1, 200 m/s, under similar loading and fracture stress [11]. Besides, it can be noticed that the velocity has never reached a steady state

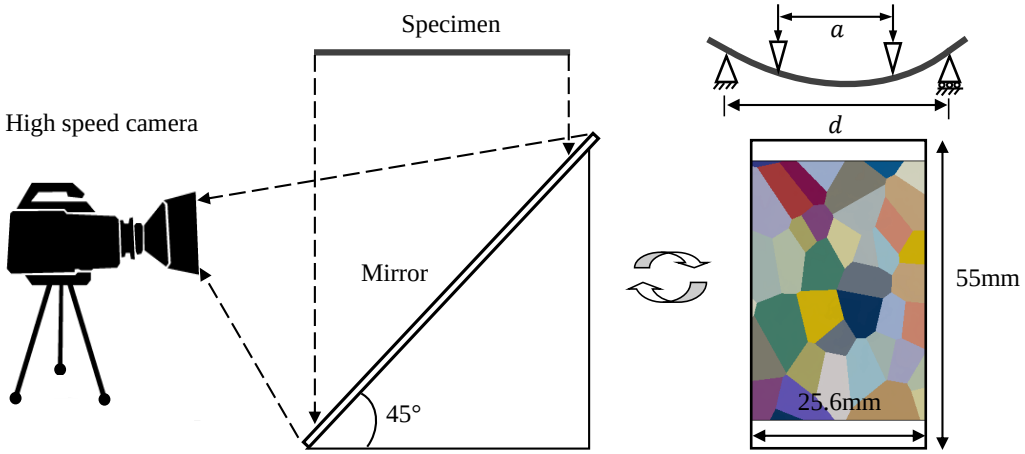

FIG. 3: Schema of the experimental set up: a tilted mirror is put under the specimen to allow the camera to view the tensile surface.

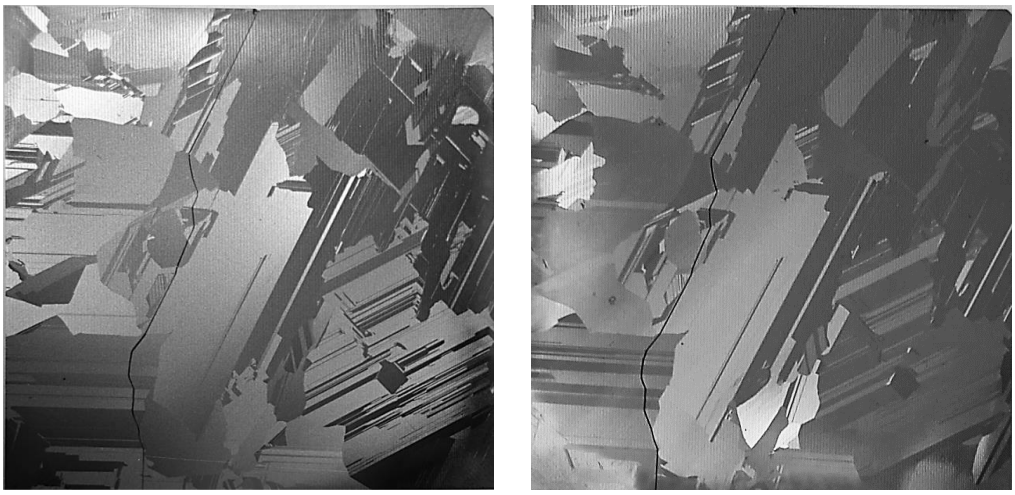

Twin plate 1 Twin plate 2

FIG. 4: Crack path of twin plates. Twin plates denote different specimens with the same grain shapes and distributions as well as grain orientations. It demonstrates that the fracture path is reproducible under the same loading conditions.

value as the crack process in single crystal [7, 11]. The averaged velocity is continuously changing from grain to grain, even sometimes extremely low, which indicates that the crack has been slowed down or shortly stopped. This conclusion is in a good agreement with the findings of [26] and [33] on the fact that the grain boundary induces a barrier effect on the propagating crack. According to the dynamic propagation criterion (i.e. the Freund condition [34]), the propagation velocity has an inverse relationship with the dynamic energy release rate (also the dynamic crack propagating force). Thus, in order to overcome the grain boundary obstacle, the crack slows down to increase its driving force.

B. Fractography analysis

The crack surface provides a lot of information about the fracture process. Particularly, in bending configuration, the crack front presents a quarter ellipse and a straight line, as illustrated in Fig. 7a. Such crack profile can be identified with the presence of Wallner lines [35], according to Fréchette [36]. These roughness-induced marks permit to identify the crack propagation direction. Besides the Waller lines, it has been highlighted, specially for (111) single silicon, that a kind of instabilities initiate from dopant under bending condition [11, 14, 15]. This kind of instabilities can also be observed in multi-crystalline silicon as reported in [23],

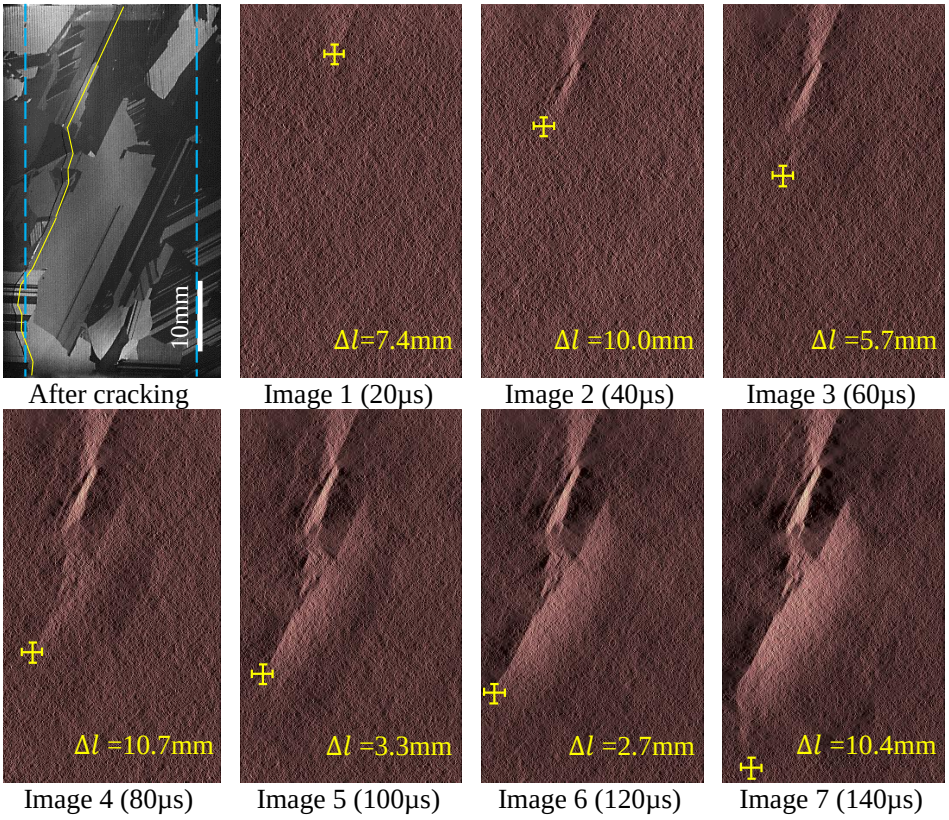

FIG. 5: Cracking process. The first image presents the completely fractured plate, the yellow lines figure out the entire fracture path and the dashed blue lines indicate the location of the inner rollers (on the punch). The second image corresponds to the subtraction between the first photo after cracking and the last photo before cracking, thus reveals the starting crack. The following images are also done by subtracting the image at the current time step by the one just before cracking. The yellow marks spot the crack tip positions in sequential subtractions, i.e. at each time step.

see Fig. 7b. The presence of the instabilities allows us to determine quickly, without any prior knowledge of the crystal orientation, that the crack surface belongs to the {111} family.

The surface imaging analysis has already revealed at the macroscopic scale the very similar fracture path for the two twin plates. In order to compare the crack surface morphology for reproducibility analysis, a confocal microscope VHX-2000F was used. Both twin plates have been investigated at the grains that are crossed by the crack. The observations are presented in Figs. 8 and 9. The overall reconstitution shows the crack surface associated with the corresponding grains. The concerned grains are numbered in the order of the crossing sequences. Particularly, the grain 9 contains many twins. Thus it has been divided into 5 parts with respect to the crack directions (the contours are clearer in Fig. 19a).

From the overall fractography displays, two main observations can be highlighted:

(i). Regarding the comparison between the two twin plates, one can notice that fracture surface morphologies are highly identical for all the grains cut by the crack. This consistency demonstrates a second time but more clearly the repeatability of the fracture behavior of multicrystalline silicon.

(ii). For both figures, some surface instabilities are clearly visible in grains 1, 2, 4, 5, 6, 9_3, 9_5, and 10, which signifies that the crack advances on the (111) plane in the above grains. For the crack surfaces of the grains 3 and 7, the instabilities are present but not outstanding, while these can not be observed for the other grains. The perturbation free surfaces will require further identification based on the grain orientation measurements.

C. Pole figure analysis

In order to further identify the cleavage planes as well as to access the grain orientations and analyze the grain boundary properties, Laue X-ray diffraction has been performed on the twin plate 1 after the fracture. This technique allows to cover relatively large specimens with respect to Electron Back-Scatter Diffraction (EBSD) analysis. It needs as input the preliminary defi-

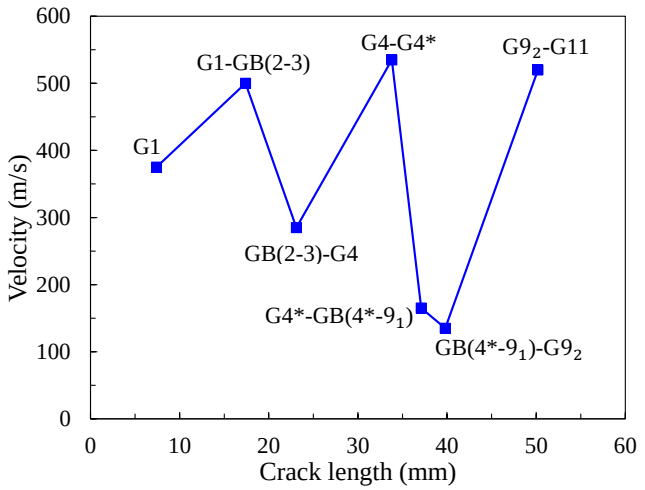

FIG. 6: Mean crack propagation velocity measured with high speed camera images, G denotes grain and GB the grain boundary. The correspondence between the grains and the numbers are reported in Fig. 8

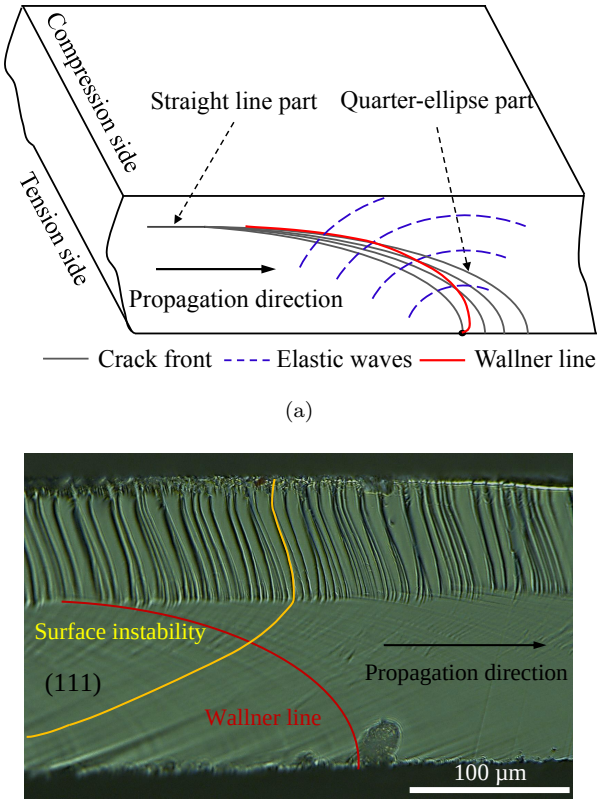

FIG. 7: Fracture surface morphology. Crack profile scheme under bending (a) and (111) surface morphology presenting Wallner lines and surface instabilities (b). The Wallner lines stem from the interaction between the crack front and the roughness induced elastic waves. The surface instabilities [15], particularly present on (111) plane, result from the crack tip deflection by the dopant atoms.

nition of the grain contours. Thanks to the different light reflections due to different orientations of the grains, the grain boundaries are visible to the naked eye. Therefore, the grain contours have been drawn thanks to the software ImageJ with a photo and then fed for orientation measurements. For comprehensiveness, the grains crossed by the crack have been figured accurately while the grains elsewhere have been drawn approximately. An angular color map is presented in Fig. 10, from which one can observe an aleatory distribution of the grain orientations. The measurements initially resulted in three angles α, γ, β that denote the rotation angles around the x, y and z axes, respectively. These angles have been used to define the Euler angles which facilitates the angle treatment (see Appendix B), especially the determination of the misorientation of a grain boundary.

The pole figure can be very straightforward expression of the cleavage plane when the latter's normal is known. Conventional pole figure takes the specimen's coordinate system as the stereo-projection basis, then one should draw at the same time crystallographic directions as well as the cleavage plane and then perform analysis to identify which directions are in this plan and which one is perpendicular to it (see section II A). However, if the cleavage plane is just chosen as the stereo-projection plane, the identification becomes much easier, knowing that the in-plane directions will certainly run across the figure contour and the perpendicular direction will be right at the figure center. Except (111) planes that have already been identified from surface instabilities, other possible planes for the mark free surfaces can be (110), (111) or (112). For the (110) plane, it contains one [110], two [111] and two [112] directions. Regarding the (111) plane, we have three [110] and three [112] directions. The (112) plane includes one [110] and two [111] directions.

In order to determine the normal direction of a fracture surface in the specimen's coordinate system, the confocal microscope has been used the measure the tilt angle with respect to a plane that is normal to the specimen's surface and contains the intersection line between the fracture surface and the specimen's surface. Another tilt angle can be directly obtained from the fracture path on the surface.

The pole figures have been carried out for the grains whose cleavage planes can not be identified by the presence of surface instabilities (see section III B). The results are presented in Fig. 11 for grains 3, 7, 8, 9_1, 9_2, and 11. The pole figure for grain 9_4 is highly identical to that for grain 9_2 and thus is not displayed. Each pole figure contains the normals of all the {110}, {111} and {112} planes which are denoted by blue circles, red squares and green triangles, respectively.

i) For the four pole sub-figures (a), (b), (c), (d), one can see that there is one [111] direction located nearby the center, while some [112] directions can also be identi-

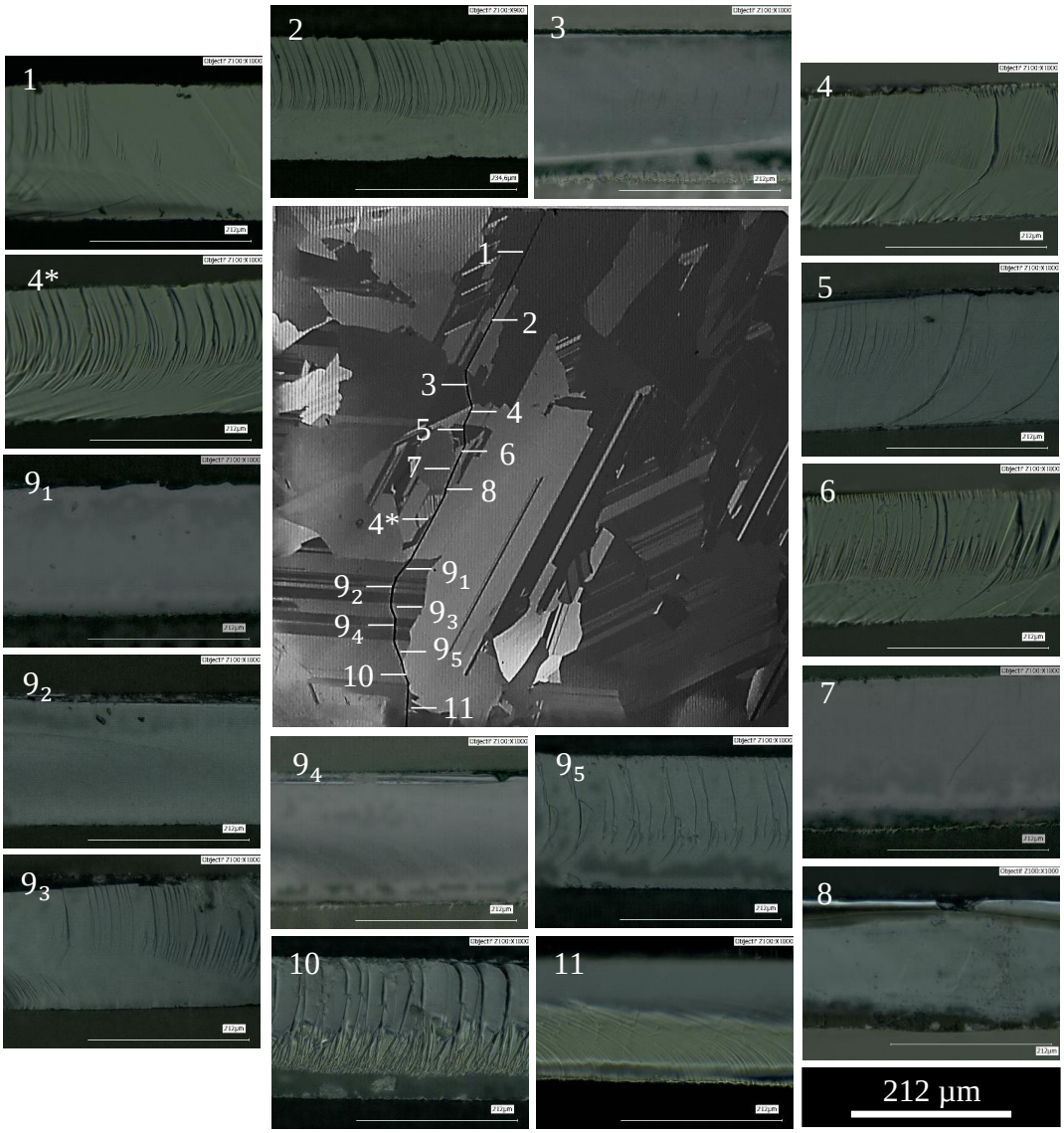

FIG. 8: Fractographies on all the fracture involved grains for twin plate 1. The numbers represent the crossing order of the crack through the grains from the beginning to the end. Note that the grain 9 owns many twins.

fied in the central region, since the closest angle between [111] and [112] directions is 19°. However, the (112) plane should be eliminated from the identification, since one can find three [112] directions close to the figure contour line, knowing that a (112) plane does not contain such directions but a (111) does. Besides, the three [110] projections located near the figure contour line confirm that the four cleavage planes belong to the {111} family.

ii) For the three other figures, they reveal in one hand one [110] direction that is close to the figure center, and in the other hand the two [111] as well as the two [112] directions that are very close to the figure contour line. One may conclude that the cleavage planes correspond to the {110} family.

Based on the above analysis, it can be concluded that the fracture in grains 3, 7, 8 and 9_1 occurs along the (111) cleavage planes while in the grains 9_2, 9_4, and 11 it happens in the (110) cleavage planes.

IV. GRAIN AND TWIN BOUNDARY CROSSING

The fracture path investigation deals with the fracture surfaces into the grains, but what happens when the crack runs through the grain boundary and nearby a twin boundary area? In section III A, it has been shown that its propagation velocity did not reach a steady state value, unlike the crack propagation in silicon single crystal. The crack velocity looks to be strongly affected by

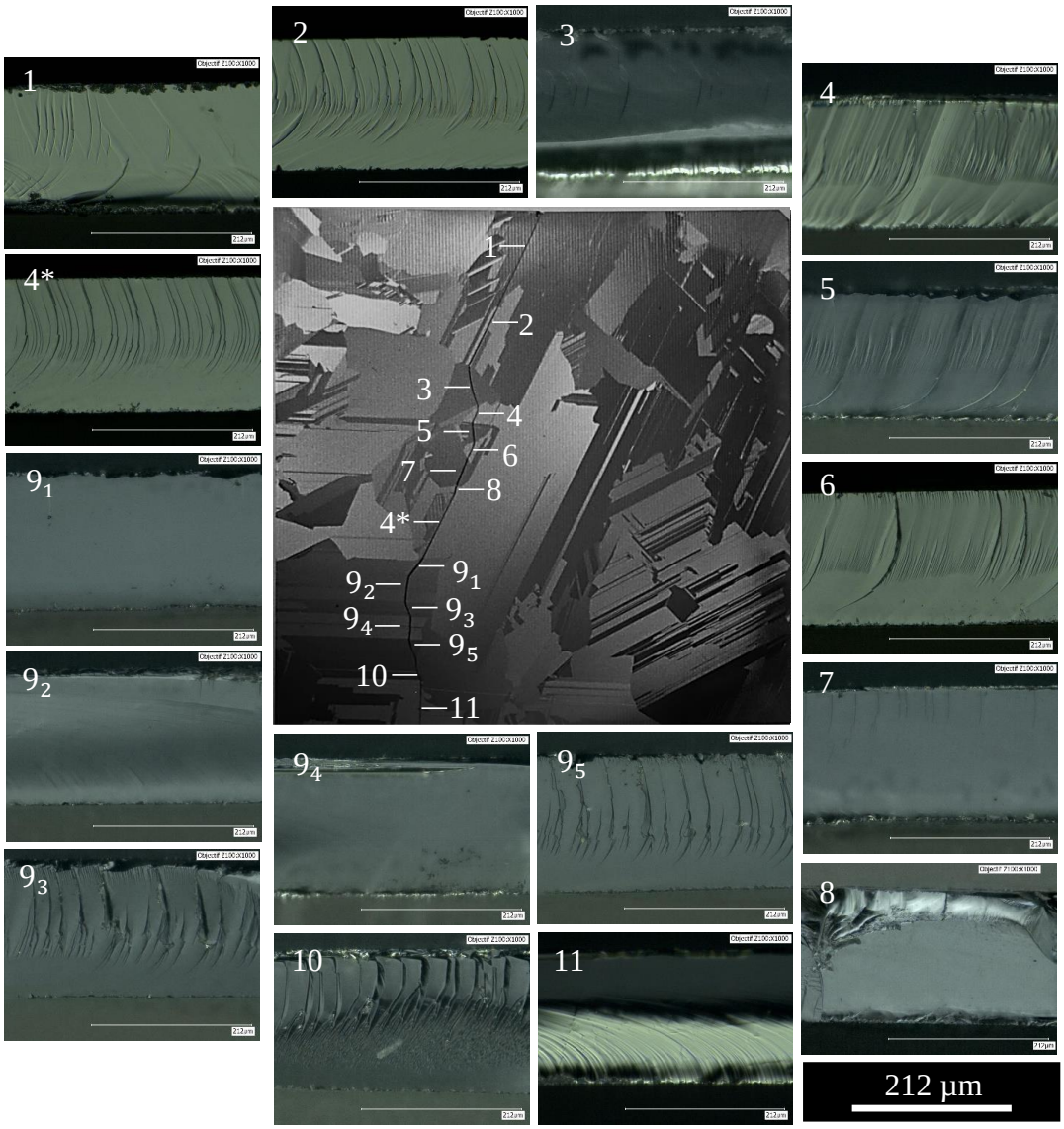

FIG. 9: Fractographies on all the fracture involved grains for twin plate 2. The numbers represent the crossing order of the crack through the grains from the beginning to the end. Note that the grain 9 owns many twins.

grain boundaries.

A. Misorientation characterization

A grain boundary can be unambiguously described by five macroscopic circles of freedom [16]: a common crystallographic axis (see Appendix C for explanation) of the two separated grains $\boldsymbol{l}$ (two DOFs), the grain level misorientation (GLMIS) angle θ that allows to bring both grains in perfect matching (one DOF), and then the boundary plane normal direction $\boldsymbol{n}$ (two DOFs), as schematized in Fig. 12. When $\boldsymbol{l}$ is perpendicular to $\boldsymbol{n}$, the grain boundary can be described by a tilt angle. When the relationship between the two vectors becomes parallel, the misorientation can be characterized by a twist angle. Generally, the grain boundary concerns a mixed characteristic. In practice, the grain level misorientation can be calculated from a rotation matrix $\underline{\underline{H}}$ represented by Euler angle triplet in reference of one grain crystallographic coordinate system. $\underline{\underline{H}}$ can be computed with the Euler rotation matrix of both grains in the reference coordinate system of the specimen (the global system) as indicated in Eq. (1).

$$\underline{\underline{H}} = \underline{\underline{R}}_{g2} . \underline{\underline{R}}_{g1}^{T} \tag{1}$$

with $\underline{\underline{R}}_{g1}$ and $\underline{\underline{R}}_{g2}$ the rotation matrix from the global system to the local crystalline systems of the two involved grains.

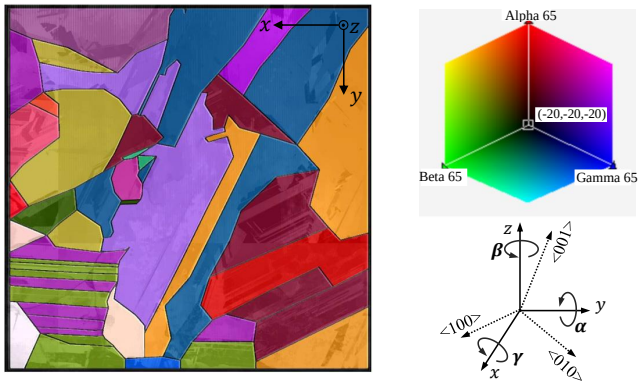

FIG. 10: Angular color map of grain orientation distribution measured with Laue X-ray diffraction. The three angles α, β, and γ denote the rotations around the x, y and z axes, respectively

The misorientation is then obtained with the expression reported in [37] and presented in Eq. (2):

$$\theta = Arcos((H_{11} + H_{22} + H_{33} - 1)/2) \quad (2)$$

In fact, due to the symmetry of cubic structure, the rotation matrix has 24 equivalent rotations which ensure the same crystalline structure (See Appendix B). In practice, one can find 24 misorientations, but only the smallest value makes sens.

With the orientations measured by the Laue X-ray diffraction, the common axes, the GLMISs as well as the angles between the common axes and the grain boundary normal have been determined and presented in Table II. The latter have been addressed in order to assess the weight of the twist and tilt angles for each GLMIS. When ξ is between 0°and 45°, the twist part is more important. Otherwise, the tilt angle occupies a greater part when ξ is between 45°and 90°. The grain boundary's normal is determined thanks to fractography, and will be detailed next. It can be noticed that the twin is associated with one of the common axes of [111] family and a GLMIS of 60°. The grains 1 and 2 have a twin relationship, their common plane is also the cleavage plane, this is why the crack does not change its propagating direction when crossing the grain boundary (see Figs. 9 and 13).

B. Grain boundary crossing

Two cleavage planes separated by a grain boundary are basically discontinuous due to GLMIS, which results in a cleavage plane level misorientation (CLMIS). Thus, when a crack arrives at a grain boundary, it should breakthrough the barrier and then propagates on the chosen cleavage plane in the grain ahead the grain boundary. Because of the discontinuity, the fracture path should be affected more or less heavily according to the CLMIS. Here, the authors differentiate the GLMIS from CLMIS since they are different in most cases (see Section IV C for the twin boundary crossing). In fracture process, CLMIS should be taken into account in grain boundary resistance analysis rather than GLMIS, as done in [28].

TABLE II: Grain boundary misorientations based on Laue X-ray diffraction measurements

Grain passage	Common axis	θ^{a} (°)	ξ^{b} (°)
1-2	$\langle 1,1,-1\rangle$	60	82
2-3	$\langle -1,1,0\rangle$	39	85
3-4	$\langle 1,0,-1\rangle$	39	67
4-5	$\langle 1,1,1\rangle$	59	3
5-6	$\langle 0,1,1\rangle$	38	61
6-7	$\langle 5,4,5\rangle$	58	64
7-8	$\langle 6,5,4\rangle$	59	21
8-4*	$\langle 1,0,1\rangle$	38	33
4*-9_1	$\langle 6,6,5\rangle$	30	2
9_1-9_2	$\langle 1,1,1\rangle$	60	2
9_2-9_3	$\langle 1,-1,1\rangle$	60	2
9_3-9_4	$\langle 1,1,1\rangle$	60	2
9_4-9_5	$\langle 1,-1,1\rangle$	60	1
9_5-10	$\langle -5,2,5\rangle$	22	62
10-11	$\langle 1,2,-2\rangle$	57	80

[a] Cleavage plane level misorientation
[b] Angle between the common axis and the grain boundary

Qiao and Chen [33] have investigated the resistance effect of the grain boundaries on the crack in tensile configuration. They have indicated that the crack front will go across the grain boundary at several breakthrough points and the persistent grain boundary islands between these points will release the crack front till a critical penetration. In the present loading configuration, 4-point bending induces a very different cracking process compared to tensile tests. As depicted in [11], the crack front covers first completely the lower (tensile) part of the specimen section and then advances toward the compression area. The crack front is illustrated in Fig. 7a. It reveals that the first breakthrough points would be nearby the specimen lower surface and that next breakthrough points would germinate progressively toward the specimen top surface (which is initially in compression).

In order to study the fracture behavior at the grain boundaries, micrographies of the crack surface in the vicinity of the grain boundaries have been carefully analyzed for one of the twin plates. The results are displayed in Fig. 13. All the crossing spots have been considered. Except the crossing at the boundary 1-2 (i.e. between grains 1 and 2) for which the two separated crystals have twin properties, two kinds of passing behaviors can be distinguished. For the boundaries 3-4, 4-5, 5-6, 7-8, 9-10, 10-11, one can observe that the crack front deflects almost from the lowest point into a non-planar area before arriving at the grain boundary. Besides, this area covers the grain boundary and looks like a 'V' shape. For the

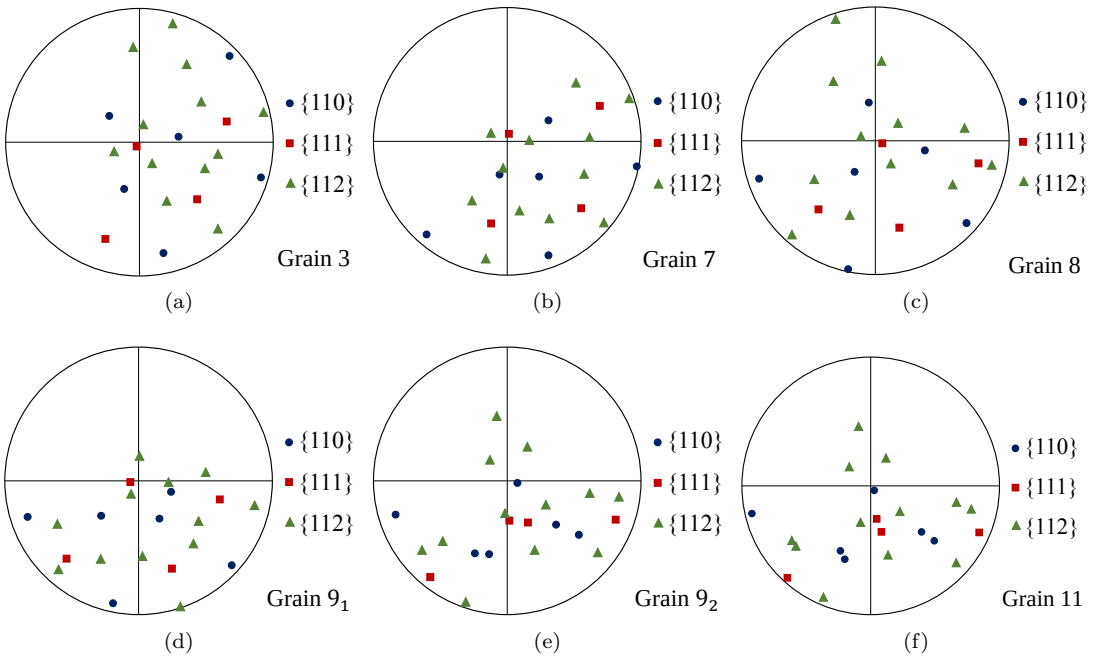

FIG. 11: Cleavage plane identification with pole figure (for {110}-blue circles, {111}-red squares and {112}-green triangles families) taking the corresponding cleavage plane as the projection plane. The pole sub-figures (a), (b), (c), (d), (e), and (f) are based on the cleavages planes of grains 3, 7, 8, 9_1, 9_2, 11 (see Fig. 9), respectively.

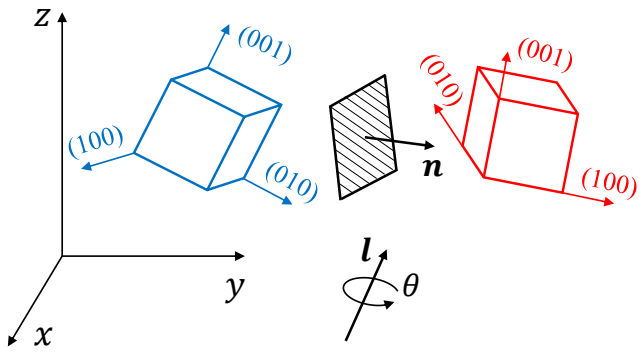

FIG. 12: Scheme of the grain boundary misorientation: the hatched plane denotes the grain boundary; $\boldsymbol{l}$ and $\boldsymbol{n}$ represent the common crystallographic axes of both grains and the normal vector to the boundary plane, respectively; θ represents the misorientation.

rest crossings, the transition region can be depicted as a 'X' shape, where the deflection begins from a middle point that is about 1/3 the thickness away from the lower surface. From the Scanning Electron Microscope (SEM) images presented in Fig. 14, one can observe the Wallner lines at the lower part ahead of the grain boundary for the two cases. The shape of Wallner lines means that the crack front is elliptical at this place thus the break points are always located at the lower surface (according to the crack front advancing description in [11]), event though the second crossing case results in deflection at a middle point. The deflection can be explained such that the CLMIS between grains leads to a disturbance of the stress field near the grain boundary. When the crack runs close to the latter, the crack front would be strongly attracted. This trapping effect sustains untill the crack continues on the proper cleavage plane after crossing the grain boundary. The difference between the two kinds of crossing behaviors is likely related to the cleavage level twist angle between the two preferential cleavage planes across the grain boundary.

The 3D morphology has been observed with a confocal microscope with a vertical moving up down every micrometer, in order to correlate the two crossing zone shapes with the misorientation. Figure 15 illustrates two representative crossing topographies, i.e. the X shape for the crossing from the grains 2 to 3, the V shape for the crossing from the grains 4 to 5. It can be observed that the X shape deflection zone correlates to two planes that make a more important twist angle, while the V shape corresponds to a smaller one. It should be mentioned that the tilt angles are very similar in these two considered crossings (see Fig. 9). Note that the grain boundary is expected to be more resistant to crack propagation when it implies a twist angle compared to a tilt angle [33]. Thus, for the second crossing behavior (X shape), one can imagine that the crack is stopped shortly at the lower front part so that the corresponding elliptical front is pinned at the straight grain boundary. As the crack velocity reduces significantly, the crack propa-

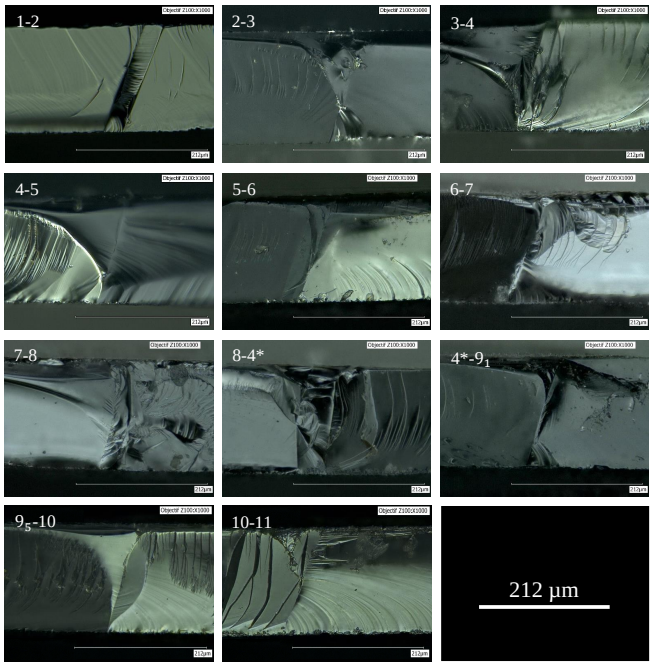

FIG. 13: Fractography on the grain boundary crossing (crack runs from the left to the right)

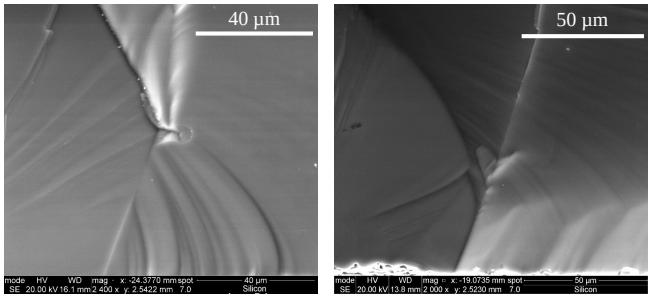

(a) (b)

FIG. 14: SEM images for grain crossing details. Zoom on the crack pattern when crossing from grains 2 to 3 (a) and from grains 4 to 5 (b).

gation force raises and releases the crack front from the lower surface to the upper surface. However, for the first crossing behavior (V shape), as the resistant effect of the grain boundary is not very important, thus the crack front passes the grain boundary almost without sudden stop.

Both crossing processes have be schematized in Figs. 16 and 17 at a grain boundary with both a tilt and a twist angles, taking into account the crack front shape for a bending test.

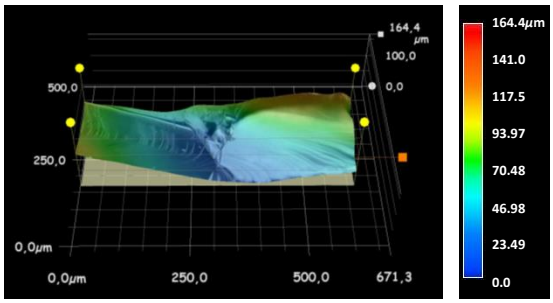

(a)

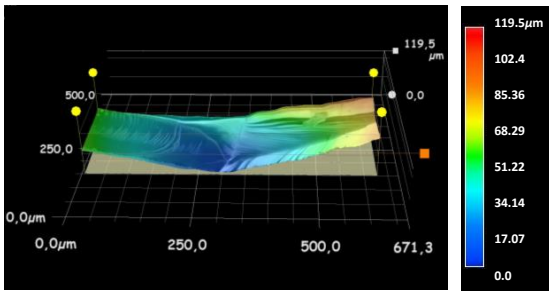

(b)

FIG. 15: Topography on the grain boundary passage: (a) Topography of the two cleavage planes across the grain boundary between the grains 2 and 3, and (b) across the grain boundary between the grains 4 and 5 . With the estimation from other topographic views that are not presented here, the twist angle in (a), approximately 30°, is more important than that in (b), approximately 12°.

C. Twin boundary crossing

The twin boundary corresponds to one of the {111} planes within a grain. For this special boundary, it is easy to identify 4 dense common axes, i.e. three [110] axes associated with a same pure tilt angle and one [111] axis associated with a pure twist angle. Using Eq. (2), the tilt and twist angles are 70.5° (coherent with the measurement in [38]) and 60° (coherent with the X-ray diffraction measurements in section IV A), respectively. However, these two angles (GLMIS) are not relevant to discontinuous angle (CLMIS) of the fracture plane across a twin boundary. According to an angular analysis, the twin boundary crossing possibilities with the smallest CLMISs are highlighted in Fig. 18. When the cleavage plane behind the twin boundary is (111), the most favorable plane ahead the twin boundary is either a (111) plane or a (110) plane (Fig. 18a). If the (111) is chosen, the associated CLMIS is a pure tilt angle since the intersection direction [110] is in the twin boundary (Fig. 18b), while if the crack propagates on a (110) plane, the associated CLMIS is a mixed angle since the intersection direction is neither in the twin boundary nor perpendicular to the latter (Fig. 18c). When the cleavage plane behind

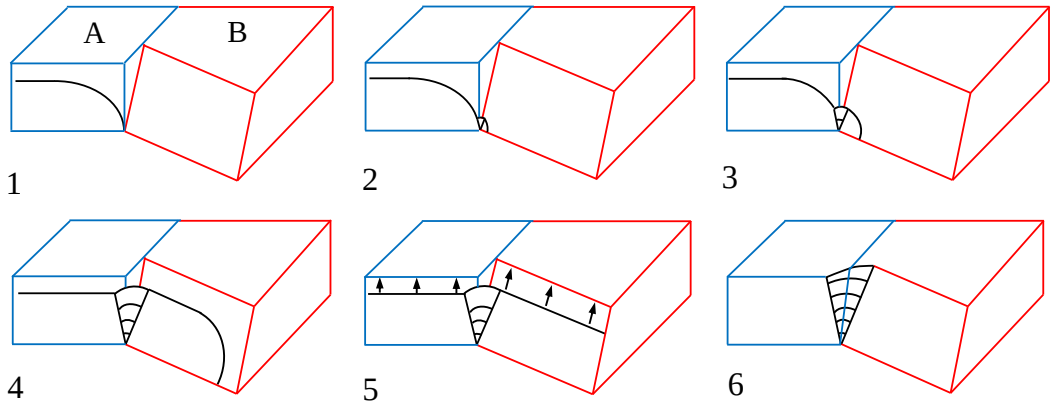

FIG. 16: Schematized process of the V crossing mechanism at a grain boundary. Grains A and B are adjacent. This crossing behavior correlates well with a relatively large twist angle between the two cleavage planes.

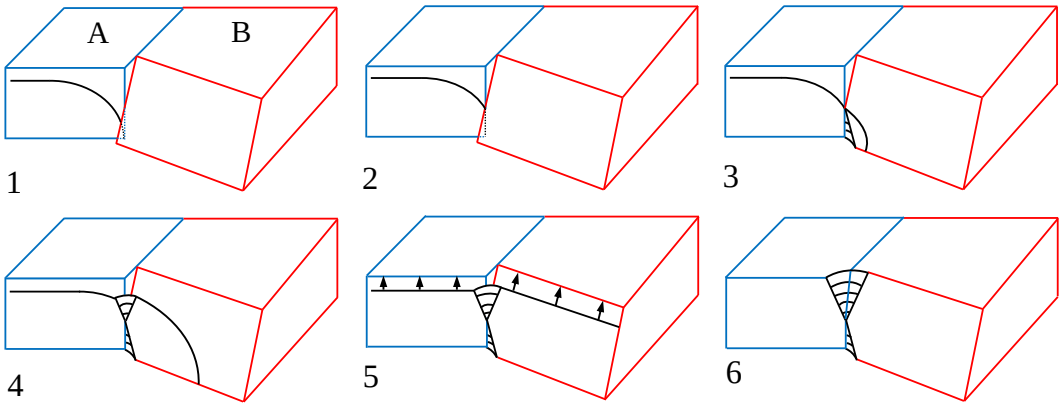

FIG. 17: Schematized process of the X crossing mechanism at a grain boundary. Grains A and B are adjacent. This crossing behavior correlates well with a relatively small twist angle between the two cleavage planes.

the twin boundary is a (110) plane (Fig. 18d), the crossing can result in a direct connection to a (110) plane (Fig. 18e) or a deflection onto a (111) plane (Fig. 18f) just like in opposite direction of Fig. 18c.

It has been indicated that in the grain $n.9$ there are several twins. In sections III B and III C, the cleavage planes have already been identified as (111), (110), (111), (110), (111) for 9_1, 9_2, 9_3, 9_4, and 9_5, respectively. The crossing morphology is illustrated in Fig. 19. From Fig. 19a, one can see that the crack in the (110) plane is almost perpendicular to the twin boundaries (we recall that each (111) plane is perpendicular to three (110) planes). The topography illustrated in Fig. 19b addresses the passage from one (110) plane to another one without remarkable deflection since the two planes are continuous. Regarding the connection from a (111) plane to a (110) plane, the topography represented in Fig. 19c reveals a mixed angle misorientation across the twin boundary. According to the measurement, we have a CLMIS of 33°around a direction tilted from the grain boundary of about 60°, which is coherent with the prediction in Fig. 18a and 18c. The analysis above highlights the difference between GLMIS and CLMIS. CLMIS is smaller than GLMIS since the grain contains more cleavage planes (6 (110) and 4 (111)) than crystalline coordinate system directions (3 (100) plane normals). Besides, the twin boundary crossing can be assimilated to the "V" shape grain boundary crossing (see Fig. 15b) and it affects more slightly the crack velocity (see Fig. 6).

V. FRACTURE MODELING

For the study of the silicon fracture behavior, the literature relies mostly on experimental observations, sometimes in light of dynamic molecular or quantum mechanical simulations to explain some specific phenomena. It should be also noted that the fully anisotropic fracture characteristics can hardly be reproduced with linear elastic fracture mechanics. In continuous mechanics a cohe-

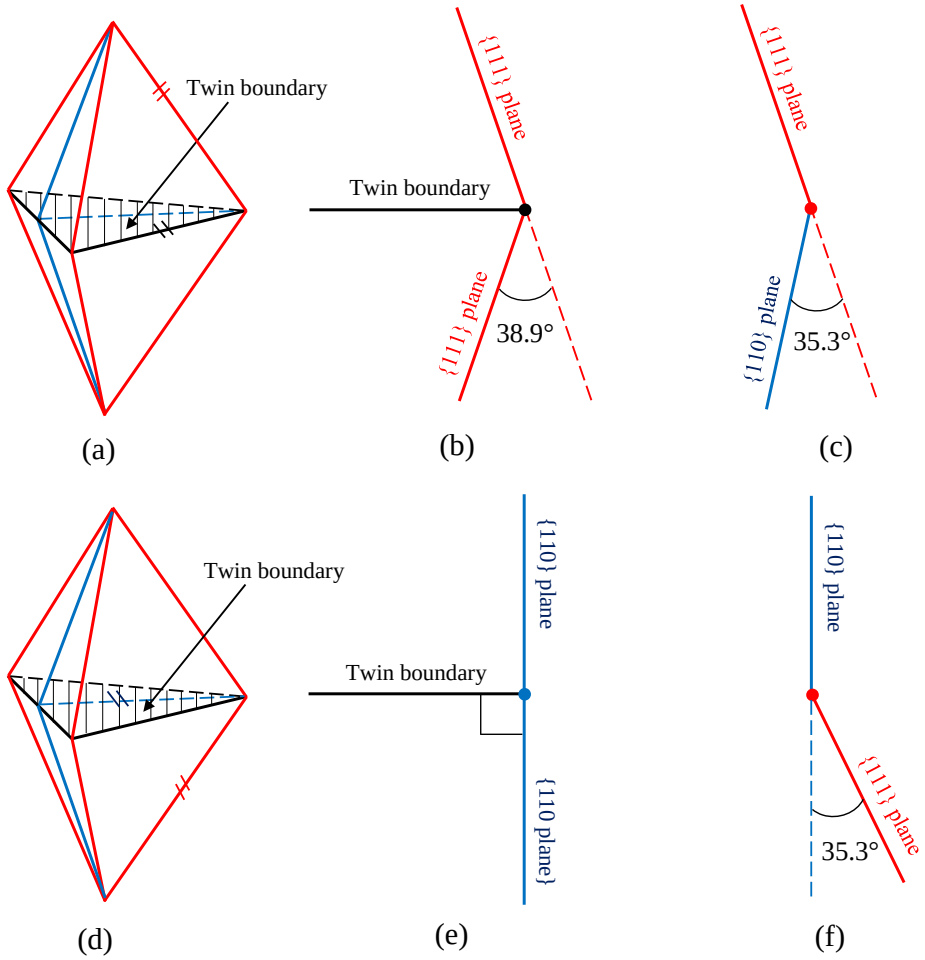

FIG. 18: Theoretical twin boundary crossing from top to bottom. The two short parallel lines in (a) and (d) indicate the intersection between the two cleavage planes with a color correspondence in (a)-(c) and another in (d)-(e).

(a) Two tetrahedrons with a common face on a (111) plane, the initial cleavage plane is another (111) plane.

(b) The crack propagates in the (111) plane ahead the twin boundary, with a pure tilt angle.

(c) The crack propagates in the (110) plane ahead the twin boundary, with a mixed tilt and twist angle since the intersection line is not in the twin boundary plane.

(d) Two tetrahedrons with a common face on a (111) plane, the initial cleavage plane is (110).

(e) The crack propagates in the same (110) plane ahead the twin boundary, with no misorientation.

(f) The crack propagates in the (111) plane ahead the twin boundary, with a mixed angle since the intersection line is not in the twin boundary plane.

sive zone model can be employed to reproduce the fracture path, similarly to the atomic debonding process, however a very small scale should be considered with respect to the characteristic cohesive length [39]. In this study, we will use the Extended-Finite Element Method (X-FEM) together with the Cohesive Zone Model (CZM) to give insight to the overall macroscopic fracture, as presented in the next section.

A. Cohesive X-FEM method

The conventional X-FEM method consists in enriching the shape functions with a Heaviside function and eventually some asymptotic functions to introduce a discontinuity in the displacement field and to faithfully represent the singular stress field around the crack tip, respectively. Concerning the X-FEM method implemented in the Abaqus software [40], the discontinuity is introduced in the way that a cohesive surface is inserted into the element when the damage initiation criterion is achieved at a given integration point [41]. Thus, the crack front can

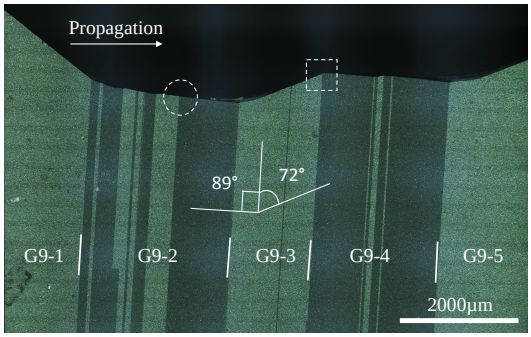

(a)

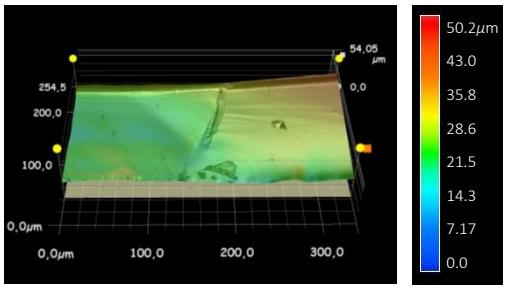

(b)

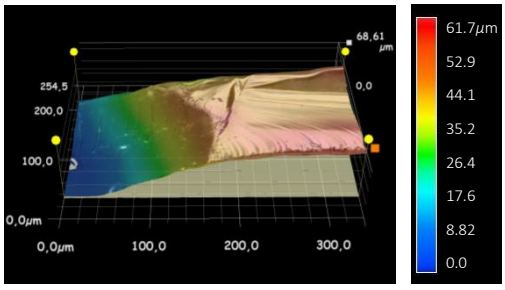

(c)

FIG. 19: Twin boundary crossing. (a) Surface observation of the twins, (b) topographies on the twin boundary crossing in 9_2 and (c) from 9_3 to 9_4, as spotted by the dashed circle and the dashed square in (a). The measured CLMISs are 2°and 33°for (b) and (c), respectively.

not stop in the element and the singular stress field is not taken into account. The fracture takes the same damage behavior as the cohesive zone. This X-FEM method is more appropriate than a pure cohesive zone model, in which the fracture path is very dependent of the mesh, knowing that it can only take place along the element boundaries. In addition, Abaqus offers to the user the possibility to define the crack initiation criterion, which suits well the modeling of anisotropic fracture behavior. It should be noted that the explicit integration scheme is not yet available for X-FEM [40] – at least till the version 6.13-4 –, and also that no crack branching can be reproduced. Therefore, in this study, only one crack propagating from a pre-crack will be simulated, with an implicit integration scheme i.e. without inertial or speed effect.

B. Damage initiation model

A damage initiation model was elaborated in Abaqus 6.13-4 User Subroutine UDMGINI in the framework of X-FEM. The initiation criterion is based on combination of the normal and tangential stresses to the potential cleavage planes σ_n, σ_{t2} and σ_{t3} in each grain. σ_{t2} and σ_{t3} correspond to the shear stresses that lead to the fracture modes II and III, respectively. The considered planes are the 4 {111} planes and the 6 {110} planes. The stress based criterion is defined in Eq. (3):

$$\delta_1.\delta_2.[< \sigma_n >^2 + (\delta_3.\sigma_{t2})^2 + (\delta_4.\sigma_{t3})^2] = \sigma_c^2 \qquad (3)$$

<> denotes Macaulay brackets with the usual interpretation. They are used here to signify that a pure compressive stress state does not initiate damage. δ_1, δ_2, δ_3, δ_4 will be justified in the discussion that follows.

It should be noted that the tangential components should be rigorously taken into account in the fracture behavior, with weight coefficients δ_3 and δ_4 greater than 1. As indicated by Kozhushko et al. [42] and Kozhushko and Hess [43], the shear stress can play a more important role than the tensile stress in the cleavage initiation of crystalline silicon. Quantitatively, ab initio calculations [44] have resulted in an ideal tensile stress of 22 GPa and an ideal shear strength of 6.8 GPa for cleveage in the (111) plane. Often in our experiments it has been observed that the crack path is sometimes far away from the maximal stress plane, implicating that the plate undergoes a mixed mode fracture, for instance where the in-plane shear stress is significant. Thus, δ_3 and δ_4 have been set to 3 in the elaborated criterion according to the ab initio calculations. In order to have a stress criterion assimilated to the energy one, the cleavage surface inclination is taken into account in the parameter δ_1 which is equal to $cos(ang1).cos(ang2)$, with $ang1$ and $ang2$ denoting the two inclination angles in the specimen's coordinate system. δ_2 is another penalty factor that is used across the grain boundary. It allows to consider the CLMIS and thus set as $cos(ang3)$, with $ang3$ denoting the misorientation. The (110) and (111) cleavage planes present different fracture toughness [8, 12]: 3.46 J/m^2 for the (110) planes and 2.88 J/m^2 for the (111) planes. This should be taken into account in the criterion by differentiating the two thresholds $\sigma_c^{(110)}$ and $\sigma_c^{(111)}$. Based on the relation between stress and energy release rate: $G \approx \sigma^2 l/E'$ (l standing for the crack length and E' the rigidity), the thresholds ratio is derived as $\sigma_c^{(110)}/\sigma_c^{(111)} \approx 1.1$.

When the cleavage plane is determined, the surface normal direction should be feed back to Abaqus solver to deduce the propagation direction. Since the Crystal

Cordinate System (CCS) is different from the Global Coordinate System (GCS), to each grain a Local Coordinate System (LCS) was established according to the orientation measurements. Besides, identical orthotropic rigidity matrix can be attributed to all grains thanks to the cubic symmetry of crystalline structure. The elastic constants were reported in [45], as presented below in the CCS with $\langle 100 \rangle$, $\langle 010 \rangle$, and $\langle 001 \rangle$ the axes of the reference frame:

$$\underline{\underline{C}} = \begin{pmatrix} 165.7 & 63.9 & 63.9 & & & \\ 63.9 & 165.7 & 63.9 & & & \\ 63.9 & 63.94 & 165.7 & & & \\ & & & 79.6 & & \\ & & & & 79.6 & \\ & & & & & 79.6 \end{pmatrix} (10^9 Pa) \quad (3)$$

The stress tensor $\underline{\underline{\sigma}}$ in the crystal coordinate system can be easily calculated when the material orientation is known:

$$\underline{\underline{\sigma}} = \underline{\underline{Q}}^T . \underline{\underline{\sigma}}_{LCS} . \underline{\underline{Q}} \quad (4)$$

where $\underline{\underline{Q}}$ is the transformation matrix from the CCS to a deviated crystal coordinate system with two axes in the potential cleavage plane (either (111) or (110)) and the third one perpendicular to this plane (i.e. the LCS). Then, the shear stresses in mode II and mode III are calculated such that σ_{t2} aligns with the intersection line between the cleavage plane and the specimen's surface and σ_{t3} in the direction perpendicular to the intersection line. However, the crack must be visualized in the GCS, so the normal direction of the crack plane in the CCS should be expressed in the GCS. To do this transformation, the following formula was applied to obtain the normal direction of the crack plane:

$$\underline{v}_n = (\underline{\underline{R}} . \underline{\underline{Q}})^T . \underline{v}_n^{(111)/(110)} \quad (5)$$

where $\underline{\underline{R}}$ represents the grain orientation with respect to the specimen's coordinate system, and $\underline{v}_n^{(111)/(110)}$ denotes the normal direction to the chosen (111) or (110) plane .

As mentioned above, the element that undergoes the damage possesses a cohesive surface. A damage evolution law is then necessary in order to obtain a real crack. In this study, the energy criterion was applied in the framework of a classic linear Traction-Separation law. The critical energy G_c corresponds to the intrinsic fracture energy of silicon measured by [8, 12]: 3.46 J/m^2 for the (110) plane and 2.88 J/m^2 for the (111) one. The linear damage evolution is applied which accounts for the mixed mode energy. So the real fracture (when the damage parameter reaches 1) takes place when the following energy relationship is satisfied:

$$G_n + G_s + G_t = G_c \quad (6)$$

C. Simulation

One can choose the Voronoi tessellation to generate aleatory grain shapes, as performed in [23]. In this study, the modeling of the real microstructure was carried out in order to compare numerical results with experimental data. The grain shape has been first reproduced thanks to a in-house Matlab code with the grain contours obtained in ImageJ, as presented in Fig. 10. The grain orientations have been obtained from Laue X-ray diffraction measurements as presented before in Section III C.

To simplify the simulation, tensile condition is considered, knowing that in bending the lower surface that undergoes pure tensile is the one where the crack initiates and propagates to the upper surface. The meshed plate as well as the boundary conditions are presented in Fig. 20. The mesh contains 31, 287 linear brick elements with reduced integration (i.e. C3D8R with 1 integration point). The crack crossed grains are meshed with elements of size 0.1 mm, whereas a global mesh size of 1 mm has been assigned elsewhere. Only one layer of elements is used for the thickness. The horizontal displacement is blocked on the left edge while a displacement is applied at the right edge. A pre-crack is introduced at the same location as for the real specimen. The simulation results are presented and compared with the experiments in Fig. 21 as well as in Table III.

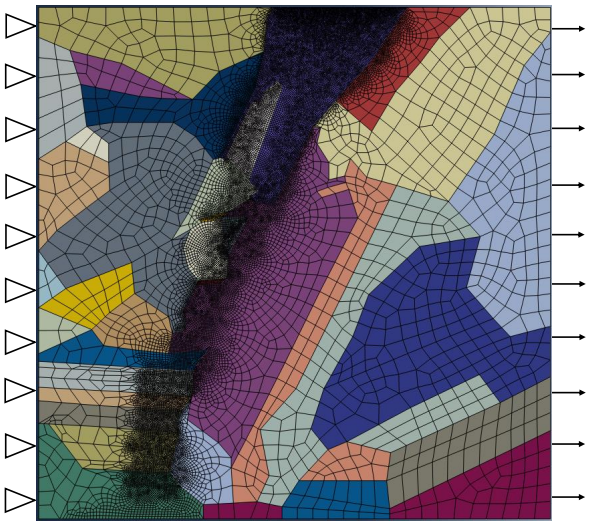

FIG. 20: Boundary conditions and mesh of the specimen

A very good agrement is found for the crack path (see Fig. 21) except for two grains nearby the bottom edge. The only difference concerns the cleavage planes in grains 9_2, 9_2, 9_4 and 11, which are detailled in Table III. The lowest energy planes are also given in this Table, giving

some insights on the expected cleavage planes from an energetical point of view. It should be noted that the simulation resulted in a consistent fracture path with the expectation – except for one grain (grain 7), while for the real experiment which is performed under pure bending loading, led to a derived path in the grains 9_2, 9_2, 9_4 and 11. In fact, these grains are located in the region either under the punch roller or out of the inner span (see Fig. 5). Thus, the local inconsistency is likely related to the disturbed stress field due to the contact stress and the stress gradient out of the inner span. Note also that the experimental and numerical cleavage planes are the same in grain 7, however it differs from the lowest energy plane. This point will be addressed in the next section.

TABLE III: Comparison of the cleavage planes between the experiment and the simulation, the differences are underlined in bold font

Grain	Experiment	Simulation	Lowest energy plane
1	(11-1)	(11-1)	(11-1)
2	(11-1)	(11-1)	(11-1)
3	(-111)	(-111)	(-111)
4	(11-1)	(11-1)	(11-1)
5	(11-1)	(11-1)	(11-1)
6	(11-1)	(11-1)	(11-1)
7	**(11-1)**	**(11-1)**	**(1-11)**
8	(111)	(111)	(111)
4*	(11-1)	(11-1)	(11-1)
9_1	**(11-1)**	**(1-11)**	**(1-11)**
9_2	**(110)**	**(111)**	**(111)**
9_3	(1-11)	(1-11)	(1-11)
9_4	**(110)**	**(111)**	**(111)**
9_5	(1-11)	(1-11)	(1-11)
10	(11-1)	(11-1)	(11-1)
11	**(110)**	**(111)**	**(111)**

VI. DISCUSSION

A. Reproducibility of the fracture

The reproducibility is always a very important issue for a convincing research work, especially when a complex problem is concerned. In the literature the investigations on silicon fracture is mostly limited to single crystal where one unique crack path is somehow predefined due to the anisotropic fracture characteristic. To the best of the authors' knowledge, this is the first work that investigates the fracture reproducibility of the silicon multicrystal. The prior required condition is to get twin specimens. The preparation as well as the loading should also be consistent. In this study, we investigated the solar grade multi-crystalline silicon plates which allowed to get twin specimens. The fact that the microstructure is constituted of large grains facilitates the observation and the identification of the cleavage planes.

The results presented in section III A as well as in section III B have shown at different scales the consistency of the fracture on twin specimens. The same crack trace on the specimen's surface reveals the same cleavage planes, while the similarity of the surface marks indicate that the two crack fronts have experienced the same atomic debonding.

The most important attention should be paid on the precrack location, since a small discrepancy can lead to a different crack path when crossing the smallest grains. In this present work, the mean crack propagation velocity is relatively low (measured around 400 m/s). It can be much more faster in a single crystal, i.e. up to or greater than 3000 m/s, then the crack propagation may undergo some instabilities such as local hackle regions, microbranching or macrobranching [46]. So it will be interesting to investigate the reproducibility for faster fracture in the future work.

B. Fracture path

The fracture of single crystal of silicon takes place preferentially on low energy crystallographic planes such as (111) and (110). For the case of multi-crystalline silicon, no crack along the grain boundary has been observed in this study. The authors presume that the dynamic crack front is sensitive to the perturbation or trapping effect induced by some material defects. The grain boundary is a complicated structure and concentrates dislocations, therefore the propagation in this region is highly unstable and it is why it is barely observed experimentally.

The cleavage planes have been identified thanks to the observation of the fracture surface instabilities and the pole figures. The instabilities-based identification approach is reliable, since the cleavage planes with instabilities have been validated with the pole figures and it has been found that these planes are indeed the (111) planes (the verification is not presented here).

In summary, the majority of these planes belong to the {111} family. Conversely the (110) cleavage planes are found in twin regions. However, when these planes are compared with the lowest energy planes, some discrepancies have been observed in grains 7, 9_1, 9_2, 9_4, 11, as summarized in Table III. This inconsistency may rely on three mechanisms: the first is the crack propagation velocity, the second is the misorientation effect and the third is the applied stress field.

i) Effect of the crack propagation velocity: as reported in [46] and later in [11], the crack will choose a higher energy plane (3.52 J/m^2) rather than a lower energy one (3.46 J/m^2) when the propagation velocity exceeds 3000 m/s. However, in this work, the crack is relatively slow due to the important pre-crack used. The inconsistent cleavage planes are correlated with important differences on fracture energies for the experiment and the theoretical analysis, i.e. 3.95 J/m^2 versus 3.15 J/m^2 for the grain 7, 4.40 J/m^2 versus 3.12 J/m^2 for the grain 9_1,

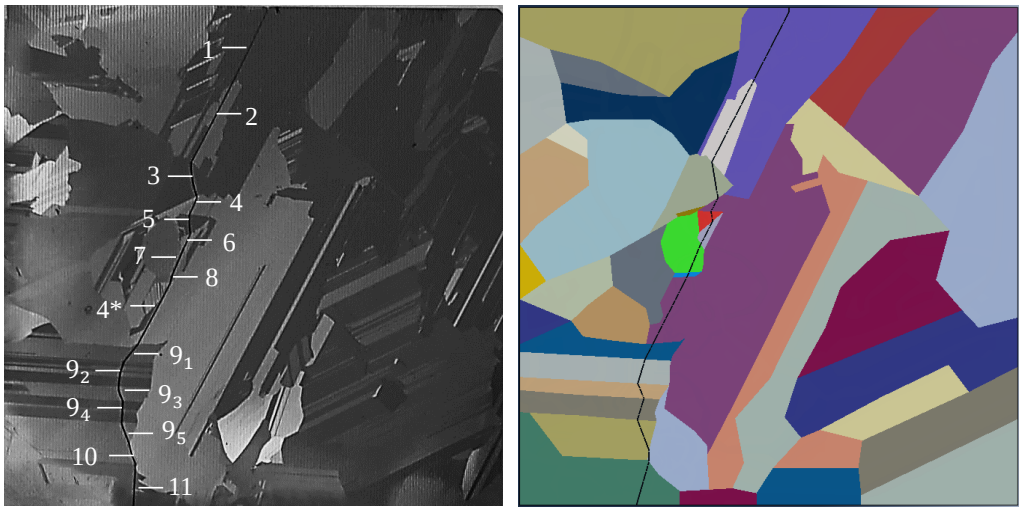

(a) (b)

FIG. 21: Comparison of the crack path between the experiment (a) and the simulation (b). The experiment was conducted in 4 point bending while the simulation was performed in uni-axial tensile.

and 3.50 J/m^2 versus 3.16 J/m^2 for grains grain 9_2, 9_4 and 11, respectively. Thus, the velocity related cleavage plane choice can be disregarded.

ii) CLMIS effect: if the planes with theoretical lowest energies were chosen, the CLMISs would eventually be very important, in our case 55°, 48°, 39°, 39°, 17°for 6-7, 4*-9_1, 9_1-9_2, 9_3-9_4, 10-11 grain boundary crossings, respectively, while these angles are 36°, 25°, 35°, 35°, 21°, with respect to the experimental cleavage planes. With the elaborated numerical model, the fracture can be well reproduced for the grains in the inner span region with the tensile simulation. The consideration of the CLMIS in the damage criterion allows to the correctly predict the (experimental) cleavage plane in grain 7, where the experimental fracture path deviates from the expectation. Here not presented, but if CLMIS is not taken into account, the simulation results in the lowest energy plane in grain 7. However, regarding other inconsistent cleavage planes, the simulation turns out the same fracture path as the expectation, which drives us to the third mechanism.

iii) Uniformity of the applied stress field: the expected cleavage planes and the simulation are performed in uniform tensile configuration, while in experiment, the crack finally runs into a stress field disturbed region (grains 9_1, 9_2, 9_4, 11), where the contact force and the stress gradient are involved. Since Abaqus provides X-FEM method only for first-order stress/displacement solid continuum elements and second-order stress/displacement tetrahedron elements [40], these two element types are not appropriate for bending simulation with a non structural mesh. Thus, only tensile loading has been considered in our simulation and further work should be done in order to verify the inconsistency root for grains in vicinity of the punch rollers.

Thus, the discrepancy can be explained by the misorientation effect and the stress perturbation around the punch rollers.

Concerning the X-FEM modeling, even if inertial effects have not been taken into account in the simulation, the model reproduced fairly well the fracture path in the region stressed uniformly (between the two inner rollers). It should be noted that the consideration of the CLMIS is important to successfully predict the cleavage plane ahead the grain boundary. The authors suppose that in multi-crystalline silicon, the mean crack velocity is relatively low, the inertial effect (which mainly disturbs the stress field) thus plays a secondary role on the cleavage plane choice compared to the surface energy and the CLMIS. More work will be required to successfully reproduce the crack path in both space and time.

C. Crack velocity and grain boundary effect

As displayed in Fig. 6, the average crack velocity varies, while a steady state of crack propagation can be attained in silicon single crystal for the same loading type (quasi-static) [9, 11]. This variation is due to the resistant effect of the grain boundaries, where the crack can be slowed down or shortly stopped in function of the misorientation.

From the grain boundary crossing fractography, a non-planar deflection region has been revealed. This region is necessary to connect two cleavage planes around the discontinuity. Chen and Qiao [28] and Qiao and Chen [33] did not observe remarkable deflection region since in their experiments the CLMIS was relatively small, while higher misorientations have been measured for our specimens. In function of the deflection morphology, two crossing behaviors can be distinguished, which are likely related

to the twist angle between the two consecutive cleavage planes. When the twist angle is important, the deflection tends to initiate from a middle thickness point (X shape), since the resistant effect is more important for a greater twist angle [29, 33] and the crack front could not penetrate the grain boundary region immediately thus is pinned on the grain boundary. Now return to Fig. 6, it can be noted that the mean velocity is small when the crack crosses particularly the grain boundaries 1-2 and 4*-9_1 where X shape deflection zones are remarkable (see Fig. 13).

Twin boundary is associated with a great GLMIS (60°). The switch of cleavage planes concerns mainly the {111} and {110} families across the boundary. However, the real GLMIS is much smaller than GLMIS, since the GLMIS addresses the three {100} planes while CLMIS relates to the four {111} and six {110} planes. In this present work, we have mainly (111)-(110) connections across the twin boundaries, however, as discussed above in Section VI B, the more favorable connection should be established only between (111) planes.

VII. CONCLUSION

In this paper, the crack propagation of two solar grade multicristalline twin samples has been investigated thanks to image analysis, fractography and microscopy. Since the grains' orientations were determined with Laue X-ray diffraction, the anisotropic fracture of multicristalline is presented by taking into account the specific orientation of each grain crossed by the crack front. A physically based X-FEM modeling has been proposed in order to successfully predict the crack path produced during these experiments. The main conclusion of this work are:

(i) Under well controlled 4 points bending solicitation it is possible, for twin specimens, to reproduce exactly the same crack path since the grain shapes as well as their crystallographic orientations are well consistent in the two specimens. The reproducibility ensures that all the observations are results of natural process and not produced by experimental hazard.

(ii) The cleavage planes encountered by these multicristalline specimens are the (111) and (110) plane families. The crack front switches from one plan to another at the grain boundary by selecting the most favorable one (most of the time (111)) in terms of not only the surface energy but also the CLMIS across the grain boundary. These results can be then well reproduced by X-FEM simulations.

(iii) The grain boundaries have an important impact of fracture propagation since the various kinds of misorientations (twist and tilt angles) produce two differents crossing mechanism. These latter namely X or V shape grain boundary crossing affect the crack velocity and therefore inhibits the crack velocity close to an average value of 400 m/s, compared with 1200 m/s of single crystal at a similar fracture stress.

Acknowledgment: The authors thank the french research agency ANR for partial funding through the DURASOL Equipex project. The authors also would like to thank Olivier Hubert from LMT Cachan for his kind help for the EBSD characterization, A. Saulot from LaMCoS INSA-Lyon for his support on confocal microscope equipment, and Amal Chabli, Paul Messaoudi and Franck Medlege from CEA/LITEN-INES for fruitful and stimulating discussions.

[1] J. Samuels and S. G. Roberts, Proc. R. Soc. Lond. A **421**, 1 (1989).
[2] M. Brede, Acta Metall. Mater. **41**, 211 (1993).
[3] B. N. Cox, H. Gao, D. Gross, and D. Rittel, J. Mech. Phys. Solids **53**, 565 (2005).
[4] A. George and G. Michot, Mater. Sci. Eng. A **164**, 118 (1993).
[5] X. Li, T. Kasai, S. Nakao, T. Ando, M. Shikida, K. Sato, and H. Tanaka, Sensor. Actuat. A-Phys. **117**, 143 (2005).
[6] M. Ohring, *The materials science of thin films* (Academic Press, 1992).
[7] D. Holland and M. Marder, Phys. Rev. Lett. **80**, 746 (1998).
[8] R. Pérez and P. Gumbsch, Acta Mater. **48**, 4517 (2000).
[9] J. Hauch, D. Holland, M. P. Marder, and H. L. Swinney, Phys. Rev. Lett. **82**, 3823 (1999).
[10] F. Ebrahimi and L. Kalwani, Mater. Sci. Eng. A **268**, 116 (1999).
[11] D. Sherman and I. Be'ery, J. Mech. Phys. Solids **52**, 1743 (2004).
[12] R. Pérez and P. Gumbsch, Phys. Rev. Lett. **84**, 5347 (2000).
[13] R. Thomson, C. Hsieh, and V. Rana, J. Appl. Phys. **42**, 3154 (1971).
[14] D. Sherman and I. Be'ery, Phys. Rev. Lett. **93**, 265501.1 (2004).
[15] L. B. Bergman and D. Sherman, Scri. Mater. **75**, 14 (2014).
[16] P. Lejček, *Grain boundary segregation in metals* (Springer-Verlag Berlin Heidelberg, 2010).
[17] M. F. Ashby, Philos. Mag. **21**, 399 (1970).
[18] D. Shilo, D. Sherman, I. Be'ery, and E. Zolotoyabko, Phys. Rev. Lett. **89**, 235504.1 (2002).
[19] M. Paggi, M. Corrado, and M. A. Rodriguez, Compos. Struct. **95**, 630 (2013).
[20] A. Infuso, M. Corrado, and M. Paggi, J. Eur. Cera. Soc. **34**, 2713 (2014).
[21] V. R. Coffman and P. S. James, Phys. Rev. B **77**, 144111 (2008).
[22] S. S. Mulay, G. Becker, R. Vayrette, J. P. Raskin, T. Pardoen, M. Galceran, S. Godet, and L. Noels, Comput. Mech. **55**, 73 (2015).

[23] L. Zhao, A. Maynadier, and D. Nelias, Int. J. Solids Struct. **In Press**, (2016).
[24] R. C. Brodie and D. F. Bahr, Mater. Sci. Eng. A **351**, 166 (2003).
[25] W. W. Gerberich, D. L. Davidson, and M. Kaczorowski, J. Mech. Phys. Solids **38**, 87 (1990).
[26] Y. Qiao and X. Kong, Mech. Mater. **39**, 746 (2007).
[27] J. Chen and Y. Qiao, Scri. Mater. **56**, 1027 (2007).
[28] J. Chen and Y. Qiao, Scri. Mater. **57**, 1069 (2007).
[29] A. Pineau, A. A. Benzerga, and T. Pardoen, Acta Mater. **107**, 424 (2016).
[30] H. J. Queisser, J. Electrochem. Soc. **110**, 52 (1963).
[31] D. Sherman, M. Markovitz, and O. Barkai, J. Mech. Phys. Solids **56**, 376 (2008).
[32] "Astm c 1161-02c,".
[33] Y. Qiao and J. Chen, Scri. Mater. **59**, 251 (2008).
[34] L. B. Freund, *Dynamic fracture mechanics* (Cambridge University Press, 1990) cambridge Books Online.
[35] H. Wallner, Z. Phys. **114**, 368 (1939).
[36] V. D. Fréchette, *Failure analysis of brittle materials: advances in ceramics* (American Ceramic Society, 1990).
[37] D. Mainprice, G. E. Lloyd, and M. Casey, J. Struct. Geol. **15**, 1169 (1993).
[38] A. Stoffers, O. Cojocaru-Mirédin, W. Seifert, S. Zaefferer, S. Riepe, and D. Raabe, Prog. Photovoltaics Res. Appl. **23**, 0042 (2015).
[39] W. J. Drugan, J. Mech. Phys. Solids **49**, 1181 (2001).
[40] *Abaqus analysis User's Guide*.
[41] J. H. Song, P. M. A. Areias, and T. Belytschko, Int. J. Numer. Meth. Eng. **67**, 868 (2006).
[42] V. V. Kozhushko, A. M. Lomonosov, and P. Hess, Phys. Rev. Lett. **98**, 195505 (2007).
[43] V. V. Kozhushko and P. Hess, Eng. Fract. Mech. **77**, 193 (2010).
[44] D. Roundy and M. L. Cohen, Phys. Rev. B **64**, 212103 (2001).
[45] J. Hall, Phys. Rev. **161**, 756 (1967).
[46] T. Cramer, A. Wanner, and P. Gumbsch, Phys. Rev. Lett. **85**, 788 (2000).

APPENDIX A. EXPERIMENTAL CURVES

The corresponding force-deflection curves for the two twin plates are presented in the below figure. Here the force stands for the total force applied on the specimen, the deflection denotes the punch's moving down distance.

If we apply the beam theory to estimate the fracture stress as presented in the below equation, the assessed values for the two twin plates are of 35MPa and of 38MPa, respectively. Indeed, the fracture behavior is quite dependent on the pre-crack. Thus, in order to guarantee the same experimental conditions, both specimens were notched with the same indentation force. The quite similar fracture stress confirm that the dimension and shape of the notches are actually close.

$$\sigma_f = \frac{3P_f(a-d)}{2bh^2}$$

where P_f is the fracture force, a and d denote the outer and inner contact spans, b and h represent the width and the thickness of the specimen.

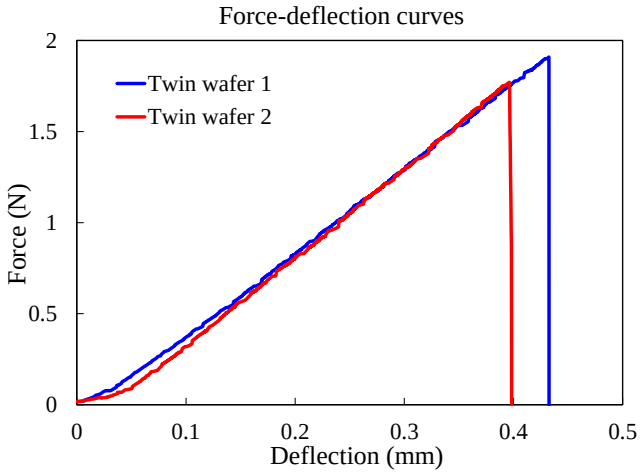

APPENDIX B. EULER ROTATION MATRIX

The Euler angle triplet follows three rotations such that the first rotation is carried out around the axis z for an angle φ, the second rotation around the new axis $x^{'}$ for χ and the third one around the updated axis $z^{'}$ for ψ. The three corresponding rotation matrix are given below:

$$\underline{\underline{R}}_z(\varphi) = \begin{pmatrix} \cos\varphi & -\sin\varphi & 0 \\ \sin\varphi & \cos\varphi & 0 \\ 0 & 0 & 1 \end{pmatrix}$$

$$\underline{\underline{R}}_{x'}(\chi) = \begin{pmatrix} 1 & 0 & 0 \\ 0 & \cos\chi & -\sin\chi \\ 0 & \sin\chi & \cos\chi \end{pmatrix}$$

$$\underline{\underline{R}}_{z'}(\psi) = \begin{pmatrix} \cos\psi & -\sin\psi & 0 \\ \sin\psi & \cos\psi & 0 \\ 0 & 0 & 1 \end{pmatrix}$$

Thus, to express the parameters (vectors, tensors etc.) of the updated coordinate system in the original coordinate system, the equivalent rotation matrix is:

$$\underline{\underline{R}}(\varphi,\chi,\psi) = \underline{\underline{R}}_z(\varphi).\underline{\underline{R}}_{x'}(\chi).\underline{\underline{R}}_{z'}(\psi)$$

For a face-centered cubic crystalline structure, we have six equivalent orthogonal axis. For axis x or $< 100 >$, one can have six possibilities, while for axis y or $< 010 >$, only 4 choices can be made in order to be orthogonal to the first axis. The axis z or $< 001 >$ is automatically

fixed by the two chosen axis. Thus, we have $6 \times 4 = 24$ equivalent structures. This notation results from the product of the transformation matrix $\underline{\underline{S}}_i$ with $\underline{\underline{H}}$:

$$\underline{\underline{H}}_i = \underline{\underline{S}}_i . \underline{\underline{H}}$$

where i=1,2,3,4,...,24 for cubic structure, $\underline{\underline{S}}_i$ allows to the cover the 24 possibilities, $\underline{\underline{H}}$ denotes the measured relative grain orientation which is defined in Section IV A.

APPENDIX C. COMMON CRYSTALLOGRAPHIC AXIS OF BOTH GRAINS SEPARATED BY GRAIN BOUNDARY

We can define the Euler angles which allows to rotate the crystalline coordinate system of one grain (first grain) into the crystalline coordinate system of the other grain (second grain). $\underline{\underline{H}}$ is then the corresponding rotation matrix. For a crystallographic axis in the second grain, $[uvw]'$, we can express it in the coordinate system of the first grain $[u^*v^*w^*]'$:

$$[u^*v^*w^*]' = \underline{\underline{H}} . [uvw]'$$

From a mathematical point of view, $[uvw]'$ and λ are one of the eigenvectors and eigenvalues of the matrix $\underline{\underline{\mathrm{H}}}$ when $[uvw]'$ can be expressed in the coordinate system of the first grain as $\lambda.[uvw]'$, with λ a constant.

Any 3×3 matrix has three eigenvalues and three eigenvectors, however for a direct rotation matrix (all the three Euler angles are not zero neither $k\pi/2$, $k = 1, 2, 3, 4$ and its determinant is equal to unity), it exists only one real eigenvalue which is equal to 1 (see the equation below) and the corresponding eigenvector has only real components. This unique real eigenvector represents the common crystallographic axis. Thus, we can define the grain boundary misorientation which brings the two grains in perfect matching by a rotation around this common axis.

Taking the rotation matrix presented in Appendix B, the equation below is used to compute the eigenvalue λ of this matrix:

$$(\lambda - 1)(\cos\varphi\cos\psi\cos\chi\lambda - \sin\varphi\cos\chi\sin\psi\lambda + \cos\varphi\cos\psi\lambda - \sin\varphi\sin\psi\lambda + \cos\chi\lambda - \lambda^2 - \lambda - 1) = 0$$

which shows that there is always an eigenvalue equals to 1.